

Contents lists available at [ScienceDirect](https://www.sciencedirect.com)

Journal of Sound and Vibration

journal homepage: [www.elsevier.com/locate/jsv](http://www.elsevier.com/locate/jsv)

# On a three-dimensional investigation of airfoil turbulence-impingement noise and its reduction by leading-edge tubercles

Georgios Bampanis <sup>a,\*</sup>, Michel Roger <sup>a</sup>, Stéphane Moreau <sup>b</sup>

<sup>a</sup> Université de Lyon, École Centrale de Lyon, INSA Lyon, Université Claude Bernard Lyon 1, CNRS, LMFA, F-69134, Écully, France

<sup>b</sup> Université de Sherbrooke, Sherbrooke, Québec, J1K2R1, Canada

## ARTICLE INFO

### Keywords:

Airfoil noise  
Noise mitigation  
Aeroacoustic propagation

## ABSTRACT

The present work addresses the turbulence-impingement noise of an airfoil and its reduction by a wavy cut of the leading edge, referred to as serrations or tubercles. It is primarily aimed at completing existing experimental databases for both straight-edge and serrated airfoils, by measurements also performed off the mid-span plane on a portion of sphere, in an open-jet anechoic wind tunnel. The three-dimensional investigation is a required condition for further applications in rotating-blade noise modeling. The turbulence is generated by a grid placed upstream of the nozzle contraction. An almost monotonically increasing reduction is found with increasing frequency, in a wide frequency range for which turbulence-impingement noise dominates, for all radiation directions. This extends observations reported in previous studies in the midspan plane only. The straight-edge results are also used to validate an analytical prediction model in a three-dimensional context. This part includes a novel correction method to account for sound refraction through the shear layers of the nozzle jet, leading to a remarkably good agreement of predictions with measurements even at shallow observer angles where the effect of the jet shear layers is significant and needs to be accounted for.

## 1. Introduction

Broadband noise generated by impinging turbulence on the leading edge of blades or lifting surfaces is a major contribution to the total noise of many airflow systems. This contribution is referred to here as turbulence-impingement or turbulence-interaction noise (TIN). It is found in low-speed fans for Heating, Ventilation and Air Conditioning (HVAC) systems, in wind turbines, as well as in aeronautical rotating-blade technology. Its reduction is therefore a crucial need for the comfort of populations. In most cases, the turbulence in the flow is an inherent condition to cope with, imposed by the installation of a fan or by its environment, thus not intrinsic to the design. Such a noise source can be mitigated with modifications of the blade shape with tubercles or serrations for instance.

The wavy airfoil leading-edge shaping, referred to as tubercles or sinusoidal serrations, has been studied as an aerodynamic and acoustic control device. Indeed, tubercles have been shown to delay stall at high angles of attack, and to sustain higher lift in the post-stall regime, thus increasing maneuverability [1,2]. Consequently, they are found to be a possible way of ensuring more robust operation of rotating-blade technology, in conditions of dynamic stall, as demonstrated, for instance, by Corsini et al. [3] and Krömer & Becker [4]. The reduction of disturbances achieved by the enhanced flow quality (suppression of separation or recirculation

\* Correspondence to: von Karman Institute for Fluid Dynamics, Waterloosesteenweg 72, 1640 Sint-Genesius-Rode, Belgium.

E-mail address: [georgios.bampanis@vki.ac.be](mailto:georgios.bampanis@vki.ac.be) (G. Bampanis).

<https://doi.org/10.1016/j.jsv.2021.116635>

Received 16 June 2021; Received in revised form 4 November 2021; Accepted 13 November 2021

Available online 29 November 2021

0022-460X/© 2021 Elsevier Ltd. All rights reserved.

**Nomenclature**

$c, e$	airfoil chord length and thickness
$c_0$	sound speed
$E$	complex Fresnel integral
$G_0, G$	free-space Green's functions, without and with flow
$h_S$	half serration depth
$k$	acoustic wavenumber $\omega/c_0$
$k_1, k_2$	chordwise and spanwise aerodynamic wavenumbers
$K_1$	modified wavenumber
$L$	airfoil span length
$\mathcal{L}, \mathcal{L}_1, \mathcal{L}_2$	Aeroacoustic transfer function
$M_0$	Mach number $U_0/c_0$
$p$	complex acoustic pressure
$R_m$	source-microphone distance
$S_0$	corrected source-observer distance
$S_{uu}$	streamwise-velocity frequency spectrum
$u_{rms}$	root-mean square turbulent velocity
$S_{pp}$	sound-pressure spectrum
$St_{h_S}$	Strouhal number based on $h_S$
$\mathbf{x} = (x_1, x_2, x_3)$	observer coordinate vector
$y_1, y_2$	chordwise and spanwise source coordinates in airfoil reference frame
$\alpha$	angle of attack
$\beta = \sqrt{1 - M_0^2}$	compressibility parameter
$\kappa, \kappa'$	modified dimensionless wavenumbers
$\lambda_S$	half serration wavelength
$\Lambda$	turbulence integral length scale
$\mu$	dimensionless frequency parameter
$\omega$	angular frequency
$\ell$	airfoil distributed unsteady lift
$\Phi_{uw}$	two-wavenumbers, upwash-turbulence spectrum
$\rho_0$	density of air
$\theta_e, \theta_c$	emission angle, total propagation angle
$\Theta, \Phi$	polar and elevation microphone angles

**Super- and subscripts**

(.)<sup>\*</sup> quantities made dimensionless by  $c/2$

...) has already an indirect benefit on noise. Yet, most of the noise reduction is achieved by acoustic interference produced by the geometrical features introduced at the leading edge, as established in numerous previous experiments. For instance, noise reductions obtained by single wavelength leading-edge serrations in a turbulent flow reach up to 8–10 dB at a certain chord-based Strouhal number for a variety of flow speeds and radiation angles [5–11].

Suitable relationships between the geometrical parameters of the periodic leading edge shape and the incident gust longitudinal wavelength have been proposed for giving highest noise reduction results. The serration amplitude has been found to be the most sensitive parameter in terms of noise reduction efficiency [6]. Surface pressure measurements along the serration tooth in the spanwise direction have shown a phase shift of the pressure fluctuations as well as weaker amplitudes compared to the baseline case [5]. This yields a destructive acoustic interference in the far-field sound [6]. A linear increase of noise reductions with the leading-edge amplitude has been found on flat plates and airfoils [6,7,12,8,11]. Moreover, an efficient ‘tuning’ of leading-edge serrations can be achieved by matching the turbulence integral length scale to half the serration wavelength maintaining the tooth hill inclination angle nearly 70°–80° [8]. Rapid decorrelation of surface pressure perturbations for high serration amplitudes is found to be the cause of noise reduction at all frequencies, whereas the peak and root local areas keep similar levels of wall-pressure fluctuations to that of the straight leading-edge counterpart. In three-dimensional Euler simulations of airfoils subjected to inflow turbulence, Kim et al. [12] also find the source cut-off effect caused by the serration obliqueness. Yet, a significant drop of coherence of wall-pressure fluctuations is found between the serration peaks and valleys [7], which is also numerically confirmed by Kim et al. [12]. Based on these observations, Chaitanya et al. [13] have introduced several innovative leading-edge

geometries (double-wavelength serrations, chopped-peak serrations, slitted-root serrations and slitted-V-root) that enhance noise reduction performances up to 4 dB compared to conventional single-wavelength serrations. A more exhaustive literature review can be found in Wang et al. [14] for instance. Yet, most of the studies have focused on sawtooth-based design in the midspan plane over limited radiation angles around the airfoils. A first objective of the present study is therefore to evaluate the possible noise reduction of wavy/sinusoidal serrations in the whole space.

Apart from the possibility of its reduction by means of serrations, turbulence-impingement noise has also motivated the development of prediction methods, that could be applied in an engineering context with acceptable trade-off between accuracy and cost. To achieve such a goal, analytical models are the best approach, especially at the early design stage. Yet, they need to be validated because of the involved simplifications made in both the geometry and the flow features. For a straight-edge airfoil, a still widely used theoretical formulation, considered in the present study, is the one proposed by Amiet [15,16], which relies on the iterative Schwarzschild's technique [17]. Amiet's model has been partly validated experimentally by measuring the noise radiation from several airfoils embedded in grid-generated turbulence, with the limitation that the investigation was restricted to the mid-span plane [15,18–20]. The second objective of this paper is to complete the validation of Amiet's model off the midspan plane. For shallow angles, this also requires considering the effect of the shear layers present in the open-jet anechoic wind tunnel. An alternative to Amiet's refraction model with a Kirchhoff's integral calculation then constitutes the third goal of this study.

The selected thin airfoil chosen in the study with long wavy serrations is shown in the next section along with the detailed experimental protocol. The way the TIN is isolated from other noise sources such as trailing-edge noise is also presented. Section 3 then describes the TIN reduction achieved by the wavy serrations in several positions around the airfoil. Section 4 then shows Amiet's three-dimensional analytical model and detailed comparisons of single-frequency three-dimensional directivity patterns. The new refraction model is also presented and the improvement achieved on the directivity plots clearly highlighted. Finally, some conclusions are drawn.

## 2. Experimental study

### 2.1. Setup and instrumentation

For convenience, airfoil turbulence-impingement noise has been thoroughly investigated experimentally for rectangular, straight-edge airfoils, in the mid-span plane (zero elevation angle). Associated analytical models have been validated accordingly. Sound radiation off the mid-span plane is seldom considered, in spite of its interest for a complete three-dimensional characterization, which is a need for relevant rotating-blade noise predictions. In fact, far-field mid-span plane investigation is partly justified by the dipolar character of the noise sources, on the one hand. It is also often the only reliable one because of the mounting of the tested airfoil between perpendicular-to-span end-plates, on the other hand. The plates cause undesired acoustic masking, reflection or scattering [21]. Even for measurements performed in the mid-span plane, corrections should be made to account for the expected reinforcement of sound due to the residual reflection of span-end sources that occurs if the plate extent is not negligible compared to the microphone distance. Yet this is never addressed in reported studies. Placing a circular-strip airfoil in the mixing layer of a round jet of same diameter is a way of indirectly address oblique radiation from the surface of an airfoil, as discussed by Roger [22]. This 'ring-airfoil' configuration is free of aforementioned spurious effects, but it required a reformulation of Amiet's theory, assuming a thin annulus instead of a rectangle. Acoustically treated end-plates, as used for instance in trailing-edge noise experiments reported by Tuinstra et al. [23], also partly prevent from the possible reinforcement of sound in the mid-span plane. But again, they do not allow off-midspan plane measurements because of the associated masking and plate-edge scattering. In the present work, the end-plates are replaced by narrow supports which make the airfoil surface directly 'visible' from a wide range of observation angles, enabling reliable measurements off the midspan plane. This is believed a good alternative to more conventional setups, in spite of the impossibility of simply varying the angle of attack.

The measurements are performed in the low-speed anechoic open-jet facility of École Centrale de Lyon. The horizontal dimensions are 5 m in the flow direction and 6 m in the lateral direction, and the height is 4 m [24]. The cut-off frequency is below 100 Hz and the overall, A-weighted background noise of about 20 dB in absence of flow. Typical sound-pressure PSD (Power-Spectral Densities) can be measured down to -10 dB above a couple of hundred Hz. A sketch of the setup is shown in Fig. 1. The three-dimensional far-field sound measurements are made with an arc antenna of 6 calibrated microphones B&K 1/2 inch, type 4189. They correspond to single-microphone measurements, because no cross-spectral analysis is performed on the associated 6 signals. The rotation is remote-controlled, around a vertical axis coinciding with the mid-chord span line of the airfoil. With this antenna, the accessible azimuth  $\theta$  ranges from  $-110^\circ$  to  $+110^\circ$ , and the accessible elevation angle  $\phi$  from  $0^\circ$  to  $75^\circ$  by steps of  $15^\circ$ . For a flat plate or a symmetric airfoil at zero angle of attack, the directivity of the radiated sound is symmetric in the left-bank and right-bank sides of the nozzle flow corresponding to both sides of the plate/airfoil. It is also symmetric with respect to the midspan plane. The quarter sphere ( $0^\circ < \theta < 180^\circ$ ;  $0^\circ < \phi < 90^\circ$ ) is enough to characterize the sound. In the present experiment, the radius of the sphere is  $R_m = 1.25$  m. The range  $110^\circ < \theta < 180^\circ$  is not accessible because of the close vicinity of the fiberglass walls of the room; furthermore, this range would suffer from pronounced sound scattering by the nozzle lips [25,26]. The elevation range  $75^\circ < \phi < 90^\circ$  has a poor interest in view of the negligible sound expected from the dipole character of the sources. For both the experimental characterization of TIN and the assessment of analytical modeling in three dimensions, the present experimental setup is considered of relevant design. Microphone positioning errors are estimated as  $\pm 1^\circ$  for angles and  $\pm 5$  mm for distances. Their effect remains below the significant measured variations. More crucially, corrections for sound-refraction effects through the jet shear-layers are needed. They are described in Section 4.2.

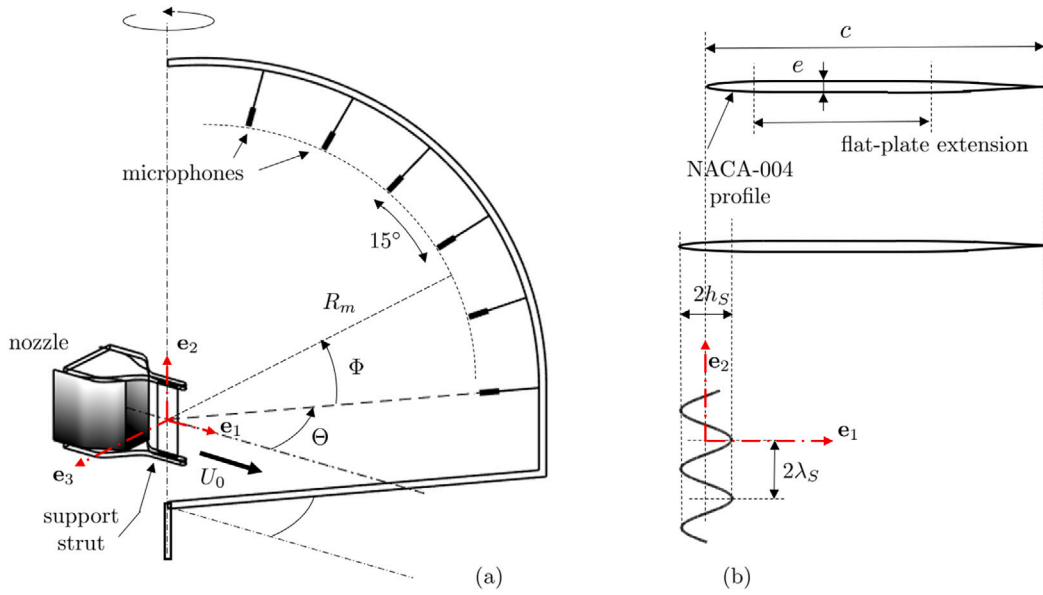


Fig. 1. (a): sketch of the experimental setup, with main notations and airfoil reference-frame axes. (b): airfoil cross-section selected for the study and serration pattern.  $h_s = 10$  mm,  $\lambda_s = 6.25$  mm,  $e/c = 3\%$ .

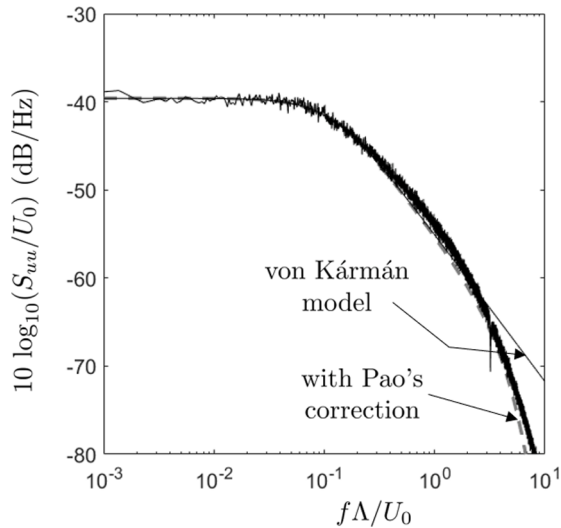


Fig. 2. PSD of the streamwise turbulent velocity, as measured by hot-wire anemometry and according to the von Kármán model. Original model and modified model with high-frequency correction as plain and dashed lines, resp.

Two airfoil shapes with the same averaged chord  $c$  of 10 cm and the same span  $L$  of 30 cm, identical to the nozzle height, have been tested. The baseline shape is a flat-plate of 3 mm thickness, completed with a sharp trailing edge and a rounded leading edge, both obtained by cutting a NACA-0004 profile at the maximum-thickness point (see Fig. 1b). The small relative thickness of 3% has been chosen in order to get as close as possible to the assumption of zero thickness made in analytical models. The modified shape, referred to as the ‘serrated’ airfoil, has a wavy leading edge, with chord extensions and reductions according to a sinusoidal pattern around the straight leading-edge position of the baseline airfoil (also shown in Fig. 1b). This makes the total chordwise extent larger but keeps the area the same, which appears as a relevant condition for a proper assessment of the effect of serrations. The serration wavelength and depth are noted  $2\lambda_s$  and  $2h_s$ . Special care has been taken to obtain a smooth surface by polishing, preventing any artificial local flow separation. However, accurate dimensional inspection of the final surface has been discarded, as not essential for turbulence-impingement noise studies. These two airfoils have been tested at mean flow velocities,  $U_0$  ranging from 19 m/s to 32 m/s, which corresponds to Reynolds numbers based on the chord length from  $1.3 \times 10^5$  to  $2.1 \times 10^5$ .

The nozzle has a contraction ratio of 2-to-1, from a square cross-section of 30 cm per 30 cm to a vertical rectangular cross-section of 30 cm per 15 cm [24]. The turbulence is generated by a grid positioned upstream of the contraction. The grid has a square mesh of size 5 cm, made of flat bars of 8 mm width. The turbulence has been measured 10 cm downstream of the nozzle exit, at the location of the airfoil leading edge but with the airfoil removed, with a single hot-wire probe. This provided the PSD of the streamwise velocity fluctuations,  $S_{uu}$  plotted in reduced form in Fig. 2, as a function of the Strouhal number based on the integral length scale  $\Lambda$ . The latter and the associated turbulent intensity  $u_{rms}/U_0$  have been determined by tuning the von Kármán model spectrum on the measurement. They are of 9 mm and 4.5%, respectively. A good fit was found, provided that a correcting factor is added to reproduce the high-frequency drop to Kolmogorov's scale in the viscous range as suggested in [27]. Even if the conditions for homogeneous and isotropic turbulence are not strictly fulfilled, the deviations from isotropy are small, with an estimated inaccuracy of about 1 dB, acceptable for the present use in airfoil-noise analytical modeling. The original expressions for  $S_{uu}$  and for the two-wavenumber spectrum of the normal velocity fluctuations (along  $e_3$ ),  $\Phi_{uw}$ , used in Section 4, read

$$S_{uu}(\omega) = \frac{u_{rms}^2 \Lambda}{\pi U_0} \left[ 1 + \left( \frac{k_1}{k_e} \right)^2 \right]^{-5/6}, \quad k_1 = \frac{\omega}{U_0},$$

$$\Phi_{uw}(k_1, k_2) = \frac{4 u_{rms}^2}{9 \pi k_e^2} \frac{\left( \frac{k_1}{k_e} \right)^2 + \left( \frac{k_2}{k_e} \right)^2}{\left[ 1 + \left( \frac{k_1}{k_e} \right)^2 + \left( \frac{k_2}{k_e} \right)^2 \right]^{7/3}}, \quad k_e = \frac{\sqrt{\pi}}{\Lambda} \frac{\Gamma(5/6)}{\Gamma(1/3)},$$

and the high-frequency correction factor is  $e^{-0.0008(k_1/k_e)^2}$ .

## 2.2. Extraction of turbulence-impingement noise spectra

The present assessment of TIN and of the effect of LE serrations on it relies on single-microphone measurements, performed in the acoustic and geometric far field. The noise reduction is obtained by simply making spectral differences between the PSD of the sound pressure measured separately with the baseline, straight-edge airfoil and with the serrated airfoil. The procedure is only valid as long as TIN dominates enough, so that other sources give a negligible contribution in terms of decibels. Two issues make this condition questionable. The first issue is that the background noise, made of the noise generated by the nozzle flow and the turbulence grid in absence of airfoil, must be subtracted in a first step, from both measurements made with the baseline and serrated airfoils. High-frequency and low-frequency limits are identified. The former results from the drop of TIN beyond a frequency limit imposed by the parameters of the turbulence grid. The latter results from undesired interaction between the jet shear-layer oscillations and the installed airfoil, leading to questionable measurements, because of the limited flow width. Therefore, an extended but limited frequency range is reliable in the experiment. The second issue is that airfoil noise also includes self-noise, essentially reduced to trailing-edge noise (TEN), and that both TIN and TEN cannot be separated in far-field measurements with single microphones. The reduction achieved by serrations can be determined by direct spectral subtraction only if TEN remains much lower than TIN. In the present experiment, the self-noise has been measured separately in clean-flow conditions ensured by removing the grid. A strip of medical tape has been stucked as boundary-layer tripping device, in order to avoid artificial tonal trailing-edge noise due to laminar instabilities. Again the corresponding background noise has been subtracted. Finally, the TIN spectra are obtained by subtracting the sound-pressure PSD of TEN to that of the total airfoil noise measured with the grid installed.

Data acquisition has been made with a resolution of 1 Hz, and a sampling frequency of 51.2 kHz. Spectra are averaged on 30 samples of 1 s, for a total acquisition time of 30 s. The subtraction procedure applied to the baseline airfoil is illustrated in Fig. 3a. After background noise subtraction, the resolution has been reduced to a bandwidth of 16 Hz to partially average out the high-frequency scatter. TEN is found well below TIN, except beyond 10 kHz. TIN spectra measured at various flow speeds are plotted in Fig. 3b, for the microphone position ( $\Theta = 90^\circ$ ,  $\Phi = 0^\circ$ ). Humps and dips are associated with chord-wise non-compactness. Their positions do not depend on flow speed. The dips occur around multiples of the chord-based Helmholtz number  $kc = 2\pi$ ,  $k = \omega/c_0$  being the acoustic wavenumber and  $c_0$  the speed of sound. When plotting the sound-pressure PSD divided by the fifth power of the flow speed  $U_0$  as a function of the chord-based Strouhal number, all spectra collapse, except for the shift of aforementioned dips and humps (see Fig. 4a). This confirms the self-similarity of the flow and of its acoustic signature, better appreciated at oblique directions, for which the spectrum envelope is more regular (Fig. 4b, for ( $\Theta = 30^\circ$ ,  $\Phi = 45^\circ$ )).

Repeating the procedure with the serrated airfoil leads to the results in Fig. 5. The spectral subtraction is quite ambiguous at high frequencies, say beyond 4 kHz, leading to higher scatter, as shown by the double arrow in Fig. 5a. Trailing-edge noise becomes dominant or of the same order of magnitude as the turbulence-impingement noise of interest, because the latter is reduced by the serrations. It must be noted that the boundary layers developing with upstream turbulence and in clean flow conditions may weakly differ, though this effect is believed of secondary importance in the present zero-loading conditions. Yet it implies that trailing-edge noise spectra might slightly differ. Moreover, TEN spectra of the serrated and baseline airfoils substantially differ, because the vortical patterns generated around the tips of the former *a priori* trigger different boundary-layer dynamics. This is emphasized by adding the self-noise spectrum of the baseline airfoil, from Fig. 3a, in Fig. 5a (red plot). Self-noise is higher for the baseline airfoil by a couple of decibels, in the range 700 Hz–7 kHz and in the very-right part of the plotted spectrum, whereas it is lower between 7 kHz and, say, 10 kHz (details are hidden by the superimposed spectra in the figure). As long as a reliable extraction of TIN can be

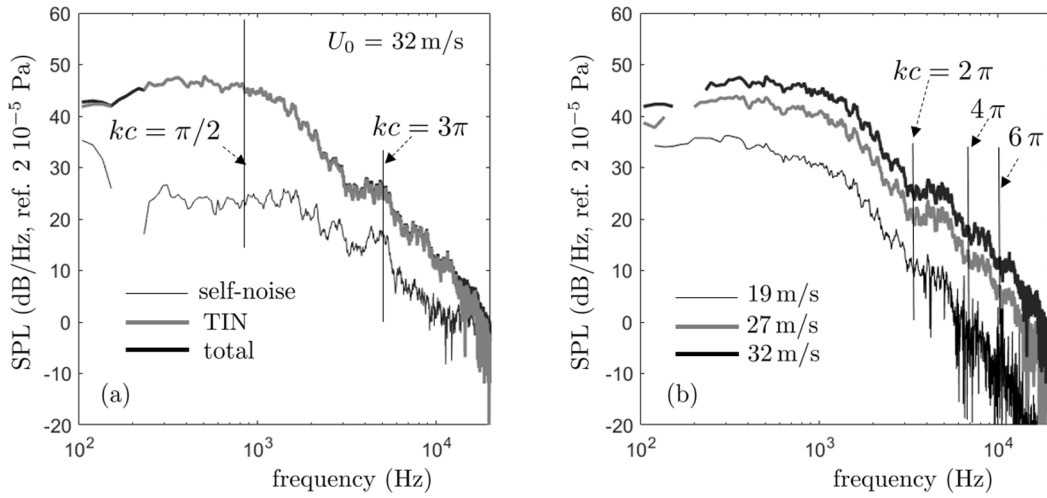


Fig. 3. Typical turbulence-impingement noise spectra of the baseline airfoil. (a): application of self-noise subtraction. (b): evidence of non-compactness dips at  $kc$  multiples of  $2\pi$ , independent of flow speed. Values  $kc = \pi/2, 2\pi, 3\pi$  and  $4\pi$  selected for further investigation.

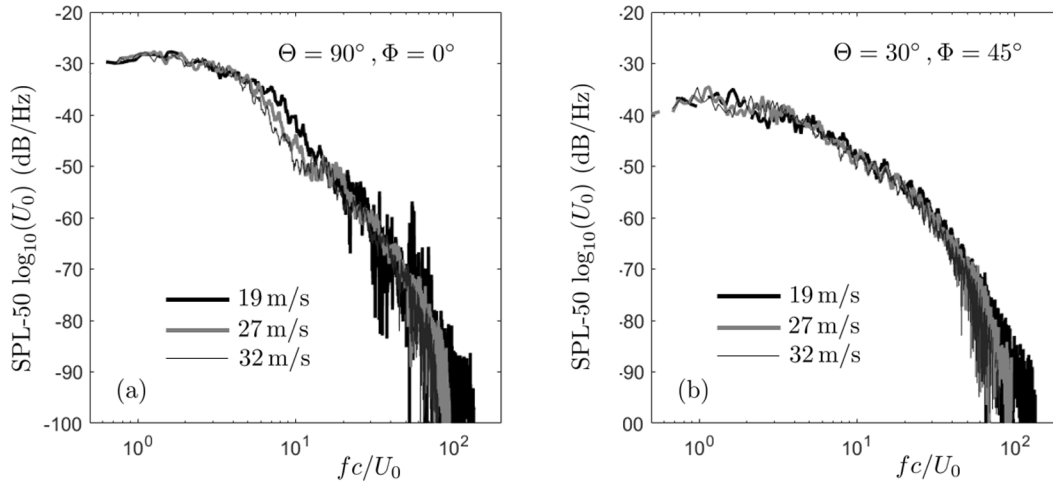


Fig. 4. TIN sound spectra, evidence of a scaling with the Strouhal number. Baseline flat-plate airfoil,  $U_0 = 32$  m/s. (a): ( $\Theta = 90^\circ, \Phi = 0^\circ$ ); discrepancies due to non-compactness dips and humps. (b): ( $\Theta = 30^\circ, \Phi = 45^\circ$ ).

performed, inspection of the serration-induced reduction makes sense. This is shown to be the case up to about 6–7 kHz in the next section, but TEN-related issues give no access to higher frequencies. The limitation would be even more crucial for thick airfoils, because leading-edge thickness is known to reduce the response to incident turbulence [28,29]. This is also why a thin airfoil is selected in this work.

An alternative approach *a priori* free of the aforementioned drawbacks is to rely on a planar microphone-array to generate a source-localization map in the plane of the airfoil. If the array-processing technique provides the power of the distributed sources, integrating the areas obviously corresponding to the leading and trailing edges on the map allows extracting each source of interest, TIN and TEN, respectively. Once this is performed for the leading-edge area and for both the baseline and serrated airfoils, the presently addressed reduction is unambiguously determined, not in terms of far-field sound pressure, but rather in terms of equivalent source power. Such an approach is described, for instance, by Bampanis et al. [11]. It is relevant at higher frequencies, for which the areas of leading-edge noise and trailing-edge noise are well separated on the source maps. This is why two techniques are combined in [11], namely far-field spectral differences for the low and middle frequencies, on the one hand, and near-field array processing for the middle-and-high frequencies, on the other hand. The second technique is discarded from the present study, because the far-field, single-microphone measurements are the only ones providing the three-dimensional radiation features of interest.

In the following, in view of the self-similarity of the flow, only the flow speed of 32 m/s is selected, for conciseness. Similar conclusions have been drawn for the other speeds.

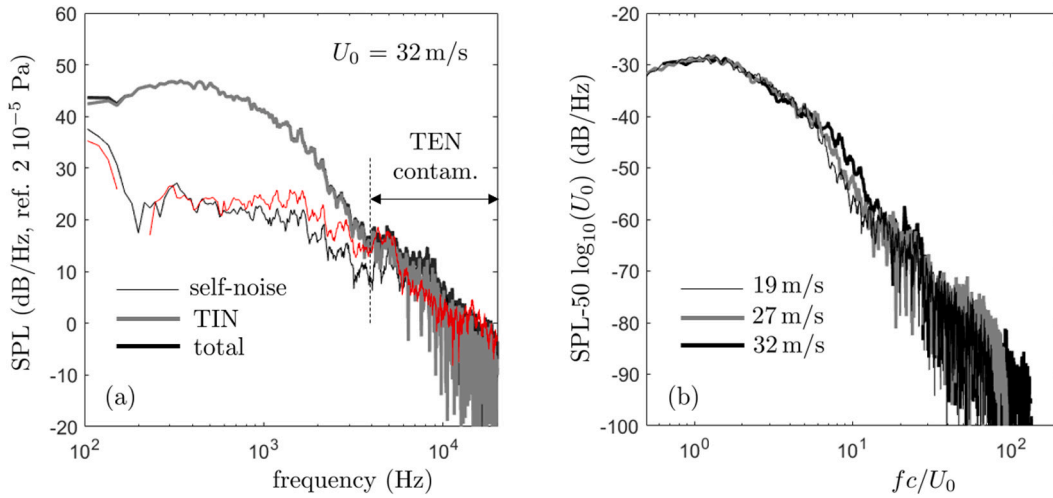


Fig. 5. Typical TIN spectra of the serrated airfoil.  $\theta = 90^\circ$ ,  $\phi = 0^\circ$ . (a): self-noise subtraction. Self-noise spectrum from Fig. 3a reproduced as the red plot, for comparison.  $U_0 = 32$  m/s. (b): evidence of a scaling with the Strouhal number. (For interpretation of the references to color in this figure legend, the reader is referred to the web version of this article.)

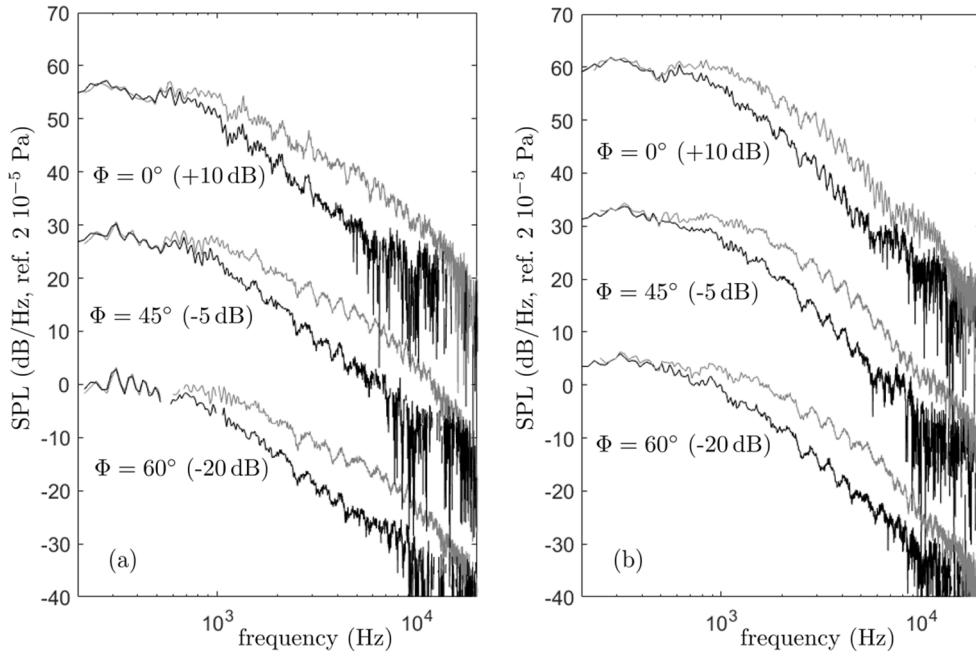


Fig. 6. Far-field sound spectra of turbulence-impingement noise for various microphone positions.  $\theta$  angles  $30^\circ$  (a) and  $60^\circ$  (b).  $U_0 = 32$  m/s. Baseline (gray) versus serrated (black). Pairs of spectra vertically shifted for clarity, by amounts indicated on the plots.

### 3. Effect of leading-edge serrations

This section presents the main results about the compared acoustic responses of the baseline and serrated airfoils introduced in Fig. 1b, for the azimuths and elevation angles selected in Section 2.1, and the flow speed 32 m/s. Far-field sound spectra are displayed in Figs. 6 and 7. For every combination ( $\theta$ ,  $\phi$ ), nearly the same reduction is observed. At very low frequencies, typically here below 300 Hz, the reduction is zero. The serrations have no effect. Beyond 300 Hz, the reduction progressively increases as frequency increases, up to values approaching 10 dB. Then the difference between the spectra of the baseline and serrated airfoils decreases, which is attributed to the limitation of the subtraction procedure discussed in the previous section.

The results show that the serrations keep the same effectiveness in reducing the sound for all explored directions, including off the mid-span plane. Though intuitive, this was to be confirmed. Indeed, one possible effect of the serrations is to modulate the

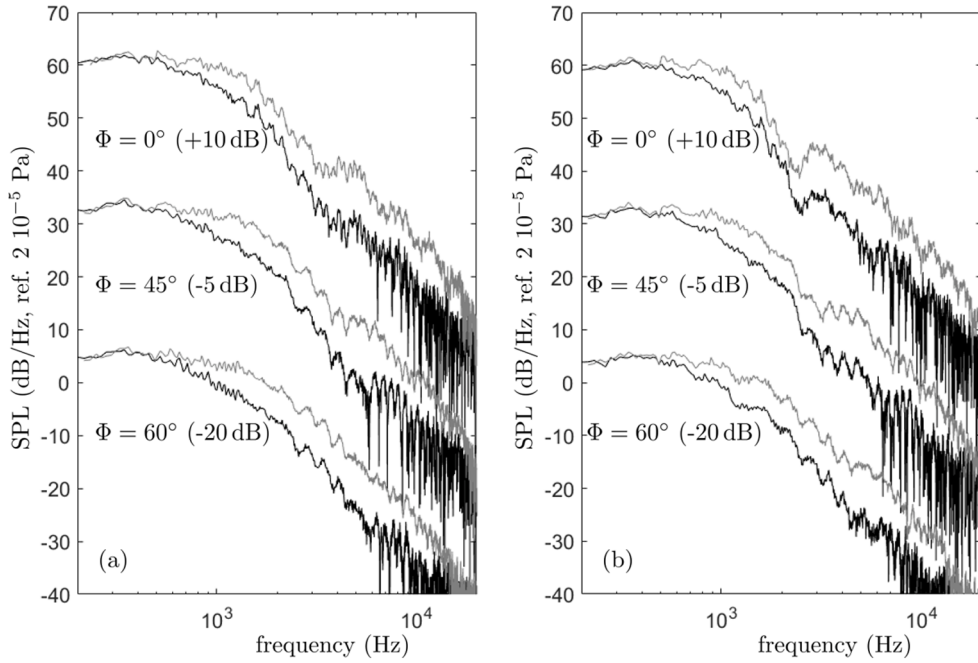


Fig. 7. Far-field sound spectra of turbulence-impingement noise for various microphone positions.  $\theta$  angles  $90^\circ$  (a) and  $110^\circ$  (b).  $U_0 = 32$  m/s. Baseline (gray) versus serrated (black). Pairs of spectra vertically shifted for clarity, by amounts indicated on the plots.

incident hydrodynamic wavenumbers. This means that special phenomena could have been expected for a spanwise wavelength  $2\pi/k_2$  coinciding with the serration wavelength. No trace of such an effect is found here.

Dimensional considerations and notions of compactness can help to analyze the observed trends. If thickness is ignored, the serration profile is defined by the wavelength  $2\lambda_S$  and the depth  $2h_S$  between tips (crests) and troughs. Any frequency of the sound is defined by the convection speed of the incident disturbances or flow speed,  $U_0$ , and the hydrodynamic wavelength  $\lambda_a = 2\pi U_0/\omega$ . The latter is related to the acoustic wavelength  $\lambda$  by  $\lambda_a = M_0\lambda$  where  $M_0 = U_0/c_0$  is the Mach number of the flow. At the present low Mach number,  $\lambda_a$  is much smaller than  $\lambda$ . A sound-source area is said acoustically compact if its characteristic size remains much smaller than the considered acoustic wavelengths. In the case of a serration period, this condition reads  $\lambda_S \ll \lambda$  or  $h_S \ll \lambda$ , depending on the direction in which compactness is assessed. For a first, heuristic analysis, a parallel gust defined by aerodynamic wavefronts parallel to the span is considered and the expected effect of serrations is inferred from the depth  $2h_S$ , points A and B being representative of a tip and a trough. Another condition, referred to as aerodynamic compactness, can be introduced as  $\lambda_S \ll \lambda_a$  or  $h_S \ll \lambda_a$ . If the pair of points AB is aerodynamically compact and if the impinging gust is of wavelength  $\lambda_a$ , a negligible phase difference is given them. Therefore, almost the same sound is expected with and without the serrations. If the pair of points is not aerodynamically compact, in contrast, both point sources partly cancel each other, with nearly no propagation-path difference as long as acoustic compactness is ensured. As a result, serrations are able to produce a significant sound reduction. Furthermore, this reduction is expected to be an increasing function of frequency, as resulting from an increasing phase shift.

For a more quantitative analysis of the reduction, the differences  $\Delta_{dB}$  between spectra of the baseline and serrated airfoils are directly plotted in Fig. 8. Results for the three values of  $\Phi$  are superimposed on each plot of a  $\theta$  value. The main trend is a nearly linear increase of  $\Delta_{dB}$  on a logarithmic frequency scale, from a low-frequency limit  $f_\Delta$ . A global empirical fit can be proposed in the form

$$\Delta_{dB} = a \frac{\log_{10}(f) - \log_{10}(f_\Delta)}{4 - \log_{10}(f_\Delta)},$$

with slightly variable values of  $a$  and  $f_\Delta$ , indicated on the plots in Fig. 8. This general behavior has been pointed out by previous investigators, for instance [6,7,12,8], who proposed the global fit in the form

$$\Delta_{dB} = 10 \log_{10}(St_{h_S}) + 10,$$

$St_{h_S} = fh_S/U_0$  being the Strouhal number based on the serration half-depth  $h_S$ . This fit is also reported in the figure as the blue line. It is found to slightly overestimate the measured reductions. Furthermore, the present adjustable fit deviates from the latter in terms of slope, especially at higher values of  $\theta$ . Here the slope of the empirical linear fit as well as the maximum achieved reduction around 10 kHz are found to decrease as  $\theta$  increases. Globally, the serration-induced reduction of TIN is larger at smaller polar angles. In Fig. 8, the frequency threshold, beyond which spurious interaction is suspected with the oscillations of the nozzle-jet shear layers, is featured by the vertical dashed lines. It remains substantially lower than  $f_\Delta$ .

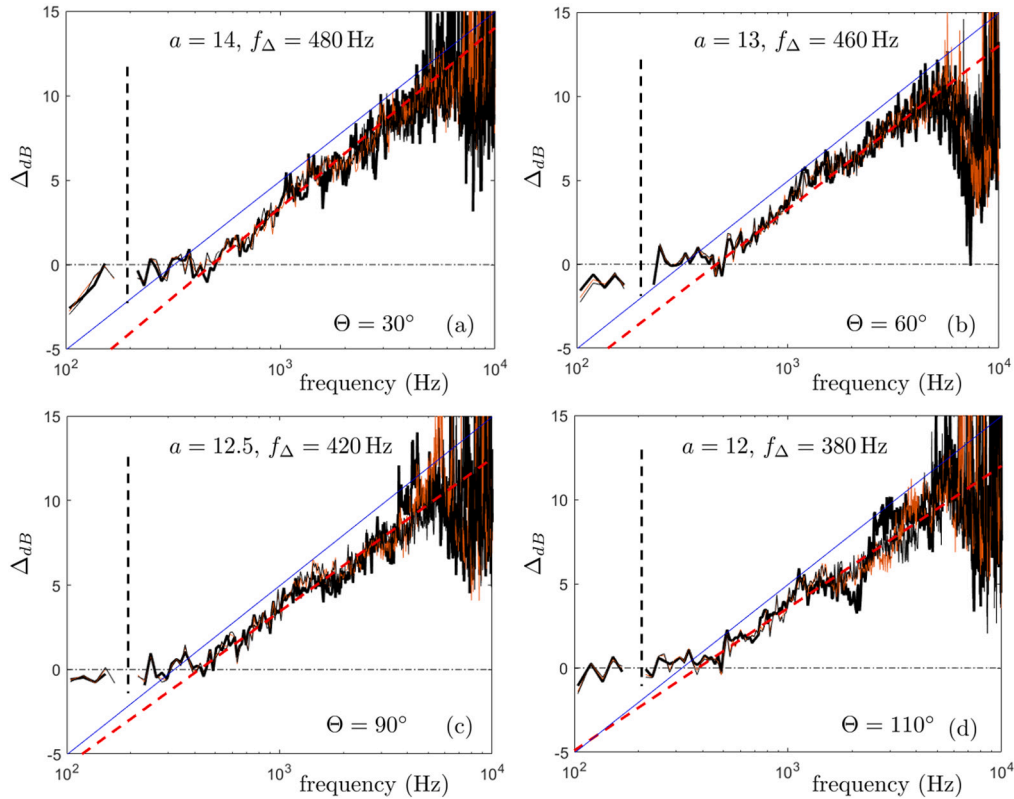


**Fig. 8.** TIN reduction spectra deduced from Figs. 6 and 7, for the four  $\Theta$  angles.  $U_0 = 32$  m/s.  $\Phi = 0^\circ$  (thick black),  $45^\circ$  (red) and  $60^\circ$  (thin black). Empirical linear fit superimposed as dashed red, with adjusted parameters  $a$  and  $f_\Delta$ . Global law  $\Delta_{dB} = 10 \log_{10}(St_{h_s}) + 10$  [6,7,12,8] added as blue line. (For interpretation of the references to color in this figure legend, the reader is referred to the web version of this article.)

Significant deviations of the sinuous measured curves from the best-tuned linear fit are observed, depending on frequency, larger as  $\Theta$  increases. Furthermore, the  $\Delta_{dB}$  plot at  $\Phi = 0^\circ$  for  $\Theta = 110^\circ$  exhibits larger oscillations than at higher elevation angles, unlike for other  $\Theta$  values. These features are attributed to the spectral dips and humps due to non-compactness. Finally, the linear fit is only an approximation. Yet it has a great interest for fast estimates in engineering context. Indeed, applications to a rotating blade are made by splitting the blade span into segments and modeling each segment as an equivalent airfoil. The aforementioned dips and humps would be largely smoothed by summing the contributions of all segments and averaging over a complete blade revolution.

#### 4. Analytical modeling of turbulence-impingement noise

##### 4.1. Amiet's model

Analytical modeling of the TIN of a straight-edge airfoil is considered in this section following Amiet's theory [16,15] based on Schwarzschild's technique. The problem is formulated in the frequency domain, in a reference frame attached to the airfoil. The latter is assimilated to a rigid flat plate of zero thickness, of chord  $c$  and span  $L$ , embedded in a uniformly moving fluid of speed  $U_0$  parallel to the chord. The model is a high-frequency approximation, addressing the compressible response of the airfoil to vortical (pressure-free) disturbances. As such, it accounts for chordwise non-compactness. It is valid as long as  $\mu = kc/(2\beta^2) > 0.4$ , with  $\beta = (1 - M_0^2)^{1/2}$ . It has been proved accurate when compared to various experimental databases [18,19,29,22]. The model is in two steps, only shortly outlined here; details are found in the references. The first step is the derivation of the distributed unsteady lift forces induced on the airfoil by incident vortical disturbances and acting as equivalent dipoles of strength  $\ell(y_1, y_2)$ ,  $y_1$  and  $y_2$  being the chordwise and spanwise coordinates on the airfoil, respectively. For this, only the velocity component normal to the airfoil is involved, and the airfoil is assumed a strip of infinite span, as featured by the gray strip in Fig. 9.

The incident disturbances, assumed frozen, are expanded in two-dimensional gusts by Fourier analysis. Each gust is characterized by chordwise and spanwise wavenumbers  $k_1$  and  $k_2$ , respectively, with  $k_1 = \omega/U_0$ . Therefore,  $\mu = M_0 k_1^*/\beta^2$ , introducing the dimensionless aerodynamic chordwise wavenumber  $k_1^* = \omega c/(2U_0)$ . In a second step, the far-field sound pressure is calculated from the unsteady lift by a radiation integral, only accounting for the actual extension of the airfoil (red rectangle in Fig. 9). Possible

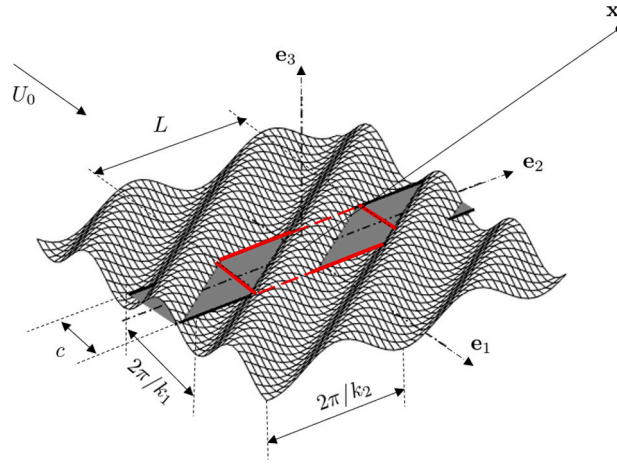


Fig. 9. Reference frame attached to a rectangular airfoil (featured in red), used in Amiet’s theory. Observer assumed in the acoustic and geometrical far field. (For interpretation of the references to color in this figure legend, the reader is referred to the web version of this article.)

end-effects are ignored. Closed-form expressions are found for the power spectral density (PSD) of the far-field acoustic pressure  $S_{pp}(\omega)$ . For arbitrary aspect ratio  $L/c$  the PSD reads

$$S_{pp}(\mathbf{x}, \omega) = \left( \frac{k \rho_0 c x_3}{2 S_0^2} \right)^2 \pi U_0 \frac{L}{2} \int_{-\infty}^{\infty} \left[ \Phi_{ww} \left( \frac{\omega}{U_0}, k_2 \right) \times \left| \mathcal{L} \left( x_1, \frac{\omega}{U_0}, k_2 \right) \right|^2 \frac{\sin^2 \left[ \left( \frac{k x_2}{S_0} - k_2 \right) \frac{L}{2} \right]}{\pi \frac{L}{2} \left( \frac{k x_2}{S_0} - k_2 \right)^2} \right] dk_2, \tag{1}$$

where  $\Phi_{ww}(k_1, k_2)$  is the two-dimensional wavenumber spectrum of the turbulent velocity component normal to the airfoil,  $\mathcal{L}$  a radiation integral accounting for chordwise non-compactness and  $S_0 = [x_1^2 + \beta^2(x_2^2 + x_3^2)]^{1/2}$  a corrected distance accounting for flow-convection effects. In the limit of large aspect ratio  $L/c \rightarrow \infty$ , an approximate expression follows from the equivalence of the sine-cardinal function with the Dirac delta function, as

$$S_{pp}(\mathbf{x}, \omega) = \left( \frac{\rho_0 k c x_3}{2 S_0^2} \right)^2 \pi U_0 \frac{L}{2} \Phi_{ww} \left( k_1, \frac{k x_2}{S_0} \right) \left| \mathcal{L} \left( x_1, k_1, \frac{k x_2}{S_0} \right) \right|^2. \tag{2}$$

This approximation selects the specific wavenumber  $k_2 = k x_2/S_0$  and perfectly focuses the radiation in the corresponding oblique direction. It is acceptable for values of  $L/c$  of about 2.5 or 3, as suggested by tests reported in the similar problem of trailing-edge noise modeling [24].

The function  $\mathcal{L}$  is derived from the local unsteady lift distribution  $\ell(y_1, y_2)$ . It has different expressions for the so-called sub-critical and supercritical gusts. For supercritical gusts, such that  $k_2^{*2} < \beta^2 \mu^2$ , it reads [22]

$$\mathcal{L}_1 = -\frac{1}{\pi} \sqrt{\frac{2}{(k_1^* + \beta^2 \kappa) \Theta_4}} e^{-i\Theta_2} E [2\Theta_4], \tag{3}$$

$$\mathcal{L}_2 = \frac{e^{-i\Theta_2}}{\pi \sqrt{2\pi (k_1^* + \beta^2 \kappa) \Theta_4}} \times \left\{ i(1 - e^{2i\Theta_4}) - (1 + i) \left[ E(4\kappa) - e^{2i\Theta_4} \sqrt{\frac{2\kappa}{\Theta_3}} E [2\Theta_3] \right] \right\}, \tag{4}$$

with  $\kappa = \sqrt{\mu^2 - (k_2^{*2}/\beta^2)}$ ,  $\Theta_2 = \mu(M_0 - x_1/S_0) - \pi/4$ ,  $\Theta_3 = \kappa + \mu x_1/S_0$ ,  $\Theta_4 = \kappa - \mu x_1/S_0$ .  $E$  is a combination of Fresnel integrals defined as

$$E(\xi) = \int_0^\xi \frac{e^{it}}{\sqrt{2\pi t}} dt.$$

For sub-critical gusts ( $k_2^{*2} > \beta^2 \mu^2$ ),  $\kappa$  is replaced by  $i\kappa'$  with  $\kappa' = \sqrt{(k_2^{*2}/\beta^2) - \mu^2}$  and the term involving the function  $(1 + i)E(4\kappa)$  by the error function  $\text{erf}(\sqrt{4\kappa'})$ . However, it is worth noting that all gusts involved in the large-aspect ratio approximation are supercritical.

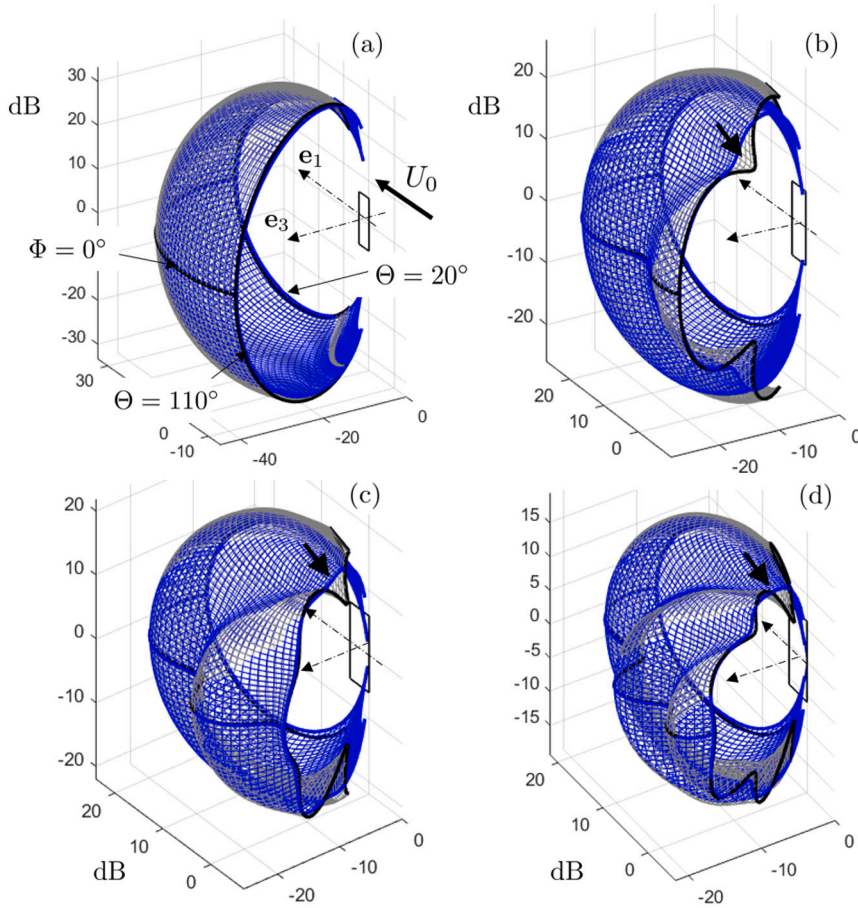


**Fig. 10.** Single-frequency, three-dimensional directivity patterns of TIN as predicted by Amiet’s model over the part of observation sphere covered by the rotating antenna in the experiment (assuming up-and-down symmetry). Left-bank side only, same decibel scale on all plots. Exact formulation (blue) versus large  $L/c$  approximation (black). Dimensionless frequency  $kc = \pi/2$  (a),  $2\pi$  (b),  $3\pi$  (c),  $4\pi$  (d). Airfoil featured by a small parallelogram on each plot. (For interpretation of the references to color in this figure legend, the reader is referred to the web version of this article.)

Sample directivity predictions with Eqs. (1) and (2) are plotted in Fig. 10, for various frequencies corresponding to Helmholtz numbers  $kc$  of  $\pi/2$ ,  $2\pi$ ,  $3\pi$ ,  $4\pi$ , respectively, at a Mach number  $M_0 = 0.095$  ( $U_0 = 32$  m/s). The bold lines feature the trace in the midspan-plane arc at  $\Phi = 0^\circ$  and the extreme meridian arcs at  $\Theta = 20^\circ$  and  $\Theta = 110^\circ$ . At the lowest frequency (Fig. 10a), the sound pattern is almost that of a dipole of axis  $e_3$ , with a wide single lobe. The parameter  $kL$  is  $3\pi/2$ , which stresses that not only the chord but also the span is nearly compact. Two azimuthal lobes (along  $\Theta$  variations) are seen at the intermediate frequencies (Fig. 10b and c) and three lobes at the highest tested frequency (Fig. 10d). In all plots, the results from the exact formulation (in blue) and from the large-span approximation (in black) are superimposed as interpenetrating meshes. The former is implemented from Eq. (1) by discretizing the integral with increments of  $k_e/50$ , the upper and lower bounds ensuring convergence. Both predictions are found to provide nearly identical results in the mid-span plane ( $\Phi = 0^\circ$ ) and around, for moderate elevation angles. The agreement holds for all emission angles at the lowest frequency (Fig. 10a). However, at higher frequencies for which the airfoil span is no longer compact, which leads to multiple lobes in the direction of the elevation angle, larger discrepancies are observed. Typically, the exact calculations have the effect of filling the dips at angles of relative extinction that are predicted with the large-span approximation. These dips are marked by thick arrows in Figs. 10b, c and d. The key outcome is that the exact formulation is needed for accurate predictions off the mid-span plane.

4.2. Corrections for shear-layer refraction

The sound path from a source point to a far-field microphone includes sound convection inside the nozzle-jet flow and propagation in air at rest outside, as illustrated in two dimensions in Fig. 11. The transmission through the shear layer of the jet causes propagation-angle deviation, so that the measurement/microphone angle  $\Theta$  differs from both the true emission angle  $\theta_e$  with respect to the fluid and the total angle  $\theta_c$  combining propagation and convection. Furthermore, the amplitude is also altered because of the opening of any acoustic beam as it is transmitted through the shear layer. This is an issue when comparing the

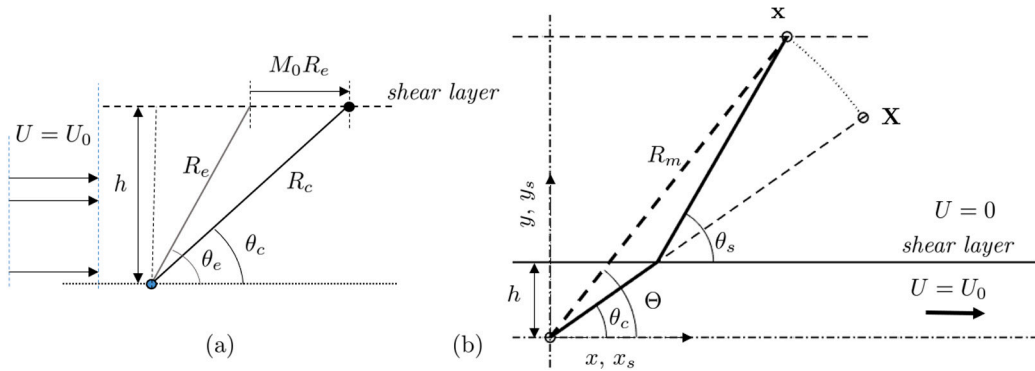


Fig. 11. Illustration of shear-layer refraction from a point source. (a): detail of convection effect; emission angle  $\theta_e$ , total angle  $\theta_c$ , actual in-flow propagation distance  $R_c$  and sound-wave transport  $M_0 R_e$ . (b): global view, featuring the microphone angle and distance ( $\Theta$ ,  $R_m$ ), the exit angle  $\theta_s$ , the microphone position  $x$  and the equivalent position  $X$  in an infinite stream.

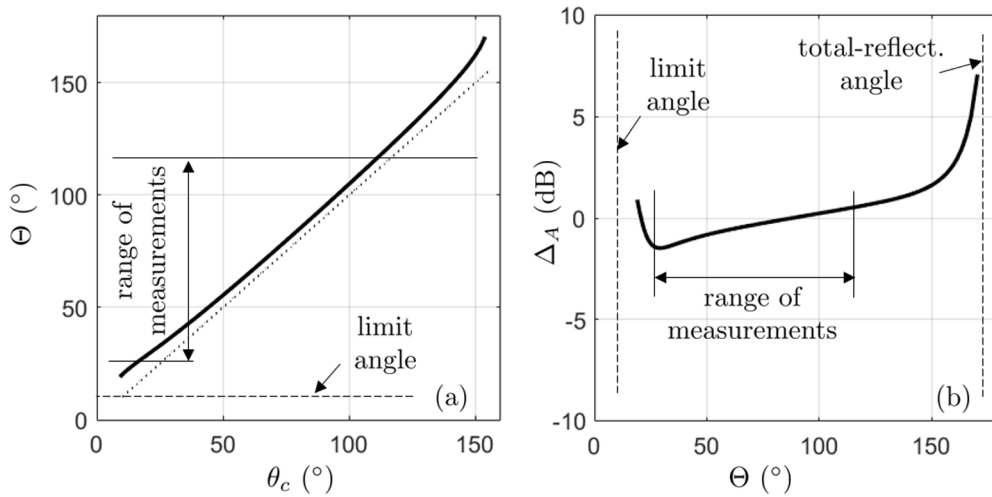


Fig. 12. Amiet's abacuses for angles,  $\theta_e$  and  $\theta_c$  (a), and amplitude (b) corrections, computed from [30] with the parameters of the present experiment.  $h = 7.5$  cm,  $U_0 = 32$  m/s,  $R_m = 1.25$  m.

measurements to predictions, because Amiet's airfoil-noise model, assuming a flow of infinite extent, involves the emission and total angles, in particular by the term

$$\frac{x_3}{S_0} = \frac{\sin \theta_e}{1 + M_0 \cos \theta_e} = \frac{\sin \theta_c}{R_c (1 - M_0^2 \sin^2 \theta_c)}$$

This is why measurements performed in open-jet wind-tunnels must be corrected or transposed. A relationship must be established between a given microphone position  $x$  and the position  $X$  that would be reached by the same sound path from the source in a flow of infinite extent. This relationship makes sense for the same source-to-microphone distance  $R_m$ , with the present measuring technique using a rotating microphone support. The passage formulae proposed by Amiet [30,31] and also discussed in Ref. [32] are often used as angle and amplitude corrections for their easy implementation. Derivation details, based on ray-tracing theory, are found in the references. The refraction deviates sound paths away from the direction of the mean flow. Therefore, the exit angle  $\theta_s$  always exceeds a limit angle  $\theta_l$  such that  $\cos \theta_l = (1 + M_0)^{-1}$ . No transmitted path can exist below this angle. Furthermore, upstream total reflection occurs for emission angles  $\theta_e > \theta_r$ , with  $\cos \theta_r = -(1 + M_0)^{-1}$ . Typical correction abacuses with indication of the angles  $\theta_l$  and  $\theta_r$  are illustrated in Fig. 12 with the parameters of the present experiment, for measurements made in the mid-span plane. The microphone angle is found very close to the emission angle  $\theta_e$ , except at lower measurement angles, as seen in Fig. 12a, whereas the total angle  $\theta_c$  is about 5° higher. Maximum amplitude corrections are of about 1 or 2 dB for the extreme angles (Fig. 12b). Despite the low value of the Mach number, below 0.1, the corrections are not negligible for these shallow angles.

Application to the present configuration might be questionable for two reasons. Firstly, equivalent airfoil noise sources are correlated sources distributed along the chord. Because the chord length is of same order of magnitude as the flow width, assuming an equivalent point source seems abusive. In fact, the shear layer is in the Fresnel zone of the airfoil, corresponding to geometrical

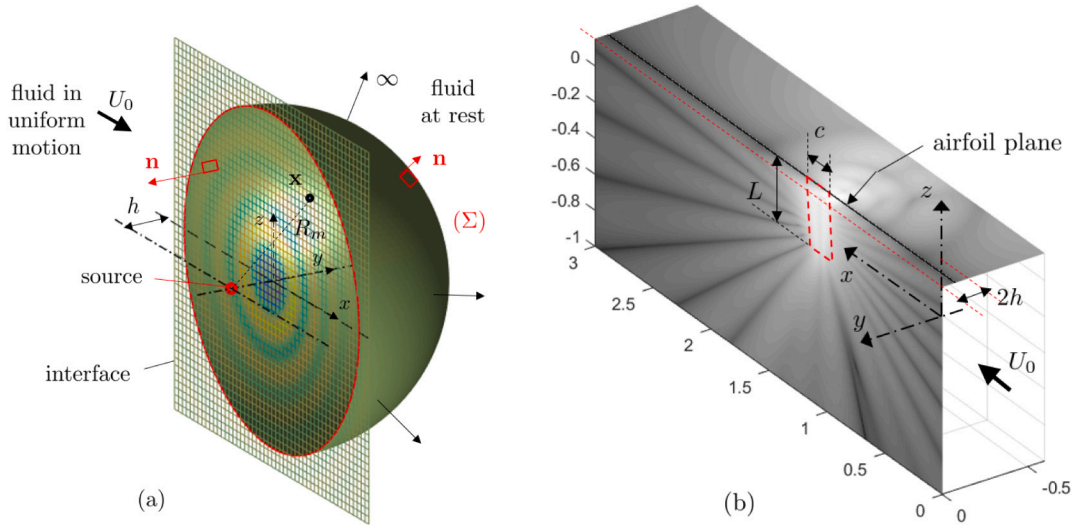


Fig. 13. (a): concept definition of a half-sphere as control surface for Kirchhoff's integral calculation; point source and observer featured as red and black points. Instantaneous pressure wavefronts illustrated on the interface. (b): double interface for application to the present experiment (coordinates in meters); indicative amplitude map on the interface, showing the incident pressure for the oblique gust focusing at  $\Phi = 60^\circ$  ( $U_0 = 32 \text{ m/s}$ ,  $kc = 4\pi$ ). Airfoil featured as red dashed rectangle. (For interpretation of the references to color in this figure legend, the reader is referred to the web version of this article.)

near field. Different refraction details are also expected at various frequencies, whereas the model corrections do not depend on frequency. Secondly, the model cannot predict any sound path below the limit refracted angle  $\theta_l$  for grazing angle of incidence in the downstream direction ( $\theta_e$  close to zero).

Another way of assessing the shear-layer refraction by the lateral nozzle-jet shear layer is chosen in the present work, made possible by the *a priori* knowledge of the sources. The initial idea, illustrated in Fig. 13a, is to assimilate the shear-layer to a planar interface of arbitrary extent and to rely on Kirchhoff's integral formulation. The latter states that the sound pressure at some frequency and at any point inside a volume ( $\mathcal{V}$ ) of air at rest, free of sources, is related to the pressure on the surface ( $\Sigma$ ) enclosing ( $\mathcal{V}$ ) by the surface integral

$$p(\mathbf{x}) = \int_{(\Sigma)} \left( G_0(\mathbf{x}, \mathbf{x}_0) \frac{\partial p(\mathbf{x}_0)}{\partial \mathbf{n}} - p(\mathbf{x}_0) \frac{\partial G_0(\mathbf{x}, \mathbf{x}_0)}{\partial \mathbf{n}} \right) d\mathbf{x}_0. \quad (5)$$

In this formula,  $\partial/\partial \mathbf{n}$  stands for the normal derivative with respect to the source coordinates, the normal unit vector pointing outward the surface ( $\Sigma$ ).  $G_0$  stands for the free-space Green's function for the Helmholtz equation in a medium at rest. In the present application, the surface ( $\Sigma$ ) can be made of the interface completed by a large half-sphere in the quiescent-air region, as shown in Fig. 13. As the half-sphere is extended to infinity, its contribution to the integral goes to zero by virtue of the Sommerfeld radiating condition and the only remaining part is the integral over the interface. This statement is only an approximation because the true shear-layer, of limited extent in the experiment, is modeled by an infinite plane separating two half-spaces, one with air at rest and the other one with air in uniform motion at the nozzle-exhaust flow speed  $U_0$ . Yet the formulation has the advantage of implicitly considering the exact wavefront structure of the incident sound on the interface.

Kirchhoff's formula is applied in two steps in the present work, for the sake of defining a correction procedure dedicated to airfoil-noise sources. At a given frequency, the latter are assumed coherent lift dipoles distributed over a flat plate of finite chord, according to Amiet's theory.

In the first step, the lift distribution is discretized into a series of elementary dipoles of chordwise and spanwise coordinates  $y_1$  and  $y_2$ , respectively, and corresponding strengths  $\ell(y_1, y_2) dy_1 dy_2$ , with axes in the direction of the unit vector  $\mathbf{e}_3$ , thus normal to both the airfoil surface and the lateral shear layer. The dipole strength of the first point at leading-edge is defined by integrating analytically the limit form of  $\ell(y_1, y_2)$  for vanishing value of  $1 + y_1^*$ , in order to account for the inverse-square root singularity. The sound-pressure density of any elementary dipole, inside the moving-fluid region mimicking the nozzle-jet, and its trace on the interface, are expressed by the scalar product of the dipole strength and of the gradient of the free-field Green's function for the convected Helmholtz equation, leading to the sound pressure

$$p_{in}(\mathbf{x}) = \ell(y_1, y_2) \frac{\partial G}{\partial y_0}, \quad \text{with} \quad G(\mathbf{x}, \mathbf{x}_0) = \frac{1}{\beta} e^{-ikM_0(x-x_0)/\beta^2} \frac{e^{ikR_s/\beta^2}}{4\pi R_s} \quad (6)$$

and  $R_s^2 = (x - x_0)^2 + \beta^2((y - y_0)^2 + (z - z_0)^2)$ , the subscript 0 standing for source coordinates in the reference frame of the interface. The normal derivative of the incident pressure in the right-hand side of Eq. (5) is defined as

$$\frac{\partial p_{in}}{\partial \mathbf{n}} = -\frac{\partial p_{in}}{\partial y} = -\ell(y_1, y_2) \frac{\partial^2 G}{\partial y \partial y_0}. \quad (7)$$

Here  $y_0 = -h$ ,  $h$  being the airfoil-to-side shear layer distance, half the flow width.

The second step, straightforward, is to derive  $\partial G_0/\partial \mathbf{n}$  from the definition

$$G_0(\mathbf{x}, \mathbf{x}_0) = \frac{e^{ikR}}{4\pi R} \quad \text{with} \quad R = |\mathbf{x} - \mathbf{x}_0|,$$

now considering that the source point  $\mathbf{x}_0$  is the field point  $\mathbf{x}$  of the first step on the interface (Eq. (6)), and that  $\mathbf{x}$  denotes the microphone position. Both steps provide a fully analytical expression of the integrand in Eq. (5), known from the direct field of the sources. The integral is computed by standard quadrature. Its full convergence may require an extent larger than the actual size of the shear layers.

The approximation made in the three-dimensional Kirchhoff formulation is relevant, only as long as the incident sound print on the interface concentrates in a small-enough area, included in the actual shear layer. This is the case for microphones in the mid-span plane, but not for measurements performed off this plane. Indeed, the large-span approximation, shown to be reliable in view of the results in Fig. 10, states that the point  $\mathbf{x}$  of coordinates ( $x_1 = R_m \cos \Phi \cos \Theta$ ,  $x_2 = R_m \cos \Phi \sin \Theta$ ,  $x_3 = R_m \sin \Phi$ ) would receive sound from the selected skewed gust of spanwise wavenumber  $k_2 = kx_2/S_0$  in a stream of infinite extent, thus

$$k_2 = k \frac{x_2}{R_m \sqrt{1 - M_0^2(x_2^2 + x_3^2)}} \simeq k \frac{x_2}{R_m}$$

at low Mach numbers for which  $M_0^2 \ll 1$ . This gust can be taken as the proper source representation to estimate the refraction with the proposed model. Its oblique radiation, first analyzed by Amiet [15], makes the dominant sound-exposed area of the interface displaced away from the mid-span plane. This motivated a dedicated implementation of the correction procedure.

Because the setup has been designed with a narrow supporting structure (see Fig. 1), the upper and lower bounds of the nozzle-jet flow can be considered also as free shear layers. Therefore, Kirchhoff's integral formula has also been applied by considering a corner-shape interface, including the vertical shear layer and the upper-side shear layer, both directly facing the microphones of the arc antenna, as depicted in Fig. 13b. The amplitude distribution of the incident sound on the interface for a microphone elevation angle of  $60^\circ$  is shown in the figure, confirming concentration around the corner and the relevance of the double-interface. Yet the approach remains an approximation. Indeed, convergence of the Kirchhoff's integral is ensured for the dimensions of the interfaces shown in Fig. 13b (coordinates are in meters), larger than the true shear layers.

#### 4.3. Directivity results

Measured directivity diagrams at the reduced frequency  $kc = 4\pi$  and for four elevation angles are plotted in Fig. 14, where they are compared to various analytical predictions. Black lines stand for predictions with the large-span approximation, Eq. (2) and the exact original Amiet's formulation, Eq. (1), both without correction for refraction. The predictions agree well in the mid-span plane but deviate from each other as the elevation angle increases. The large-span approximation (dotted black lines) features exaggerated interference dips for  $\Phi = 45^\circ$  and  $\Phi = 60^\circ$ , whereas a more regular diagram is predicted with the exact formulation (plain black lines). On overall angular shift is found for all cases, clearer when the directivity has several lobes, by the amount of about 5 dB expected from the results in Fig. 12a. Applying both corrections of this figure produces the results reported as red plain-lines in Fig. 14. The positions of the lobes are nicely recovered, but increasing amplitude errors are observed at high elevation angles ( $\Phi = 45^\circ$  and  $\Phi = 60^\circ$ ), for which the correction is not suited. Finally, the predictions made with the Kirchhoff's integral formula are plotted as thick red dashed lines. They provide the best overall agreement with the measurements. However, they also exhibit too-pronounced dips at high elevation angles. This results from the assumption of a single oblique gust as representative source, accepted for simplicity.

Results at lower frequencies are reported in Fig. 15, only retaining predictions based on Kirchhoff's formula and on the exact and corrected Amiet's model. Both provide a good overall agreement. Yet at the lowest tested frequency,  $kc = \pi/2$ , for which the airfoil is acoustically compact, Kirchhoff's formula provides a better agreement with the measured data, whereas Amiet's corrected predictions underestimate them by about 2 dB. Surprisingly, Amiet's corrections perform better at some specific angles and at the frequencies  $kc = 2\pi$  and  $kc = 3\pi$ , especially at high  $\Phi$  angles where a dip forms between two lobes ( $\phi = 45^\circ$  in Fig. 15c and  $\phi = 60^\circ$  at higher  $\Theta$  angles in Fig. 15d). Again, this is attributed to the simplification made on the source terms when applying Kirchhoff's formula. The most salient point is the general trend observed around  $\Theta = 30^\circ$  and below: Amiet's correction predicts a faster drop, as an effect of the limit angle  $\theta_l$ . At substantially higher Mach numbers,  $\theta_l$  would increase, dramatically reducing the applicability range of Amiet's formulae. In contrast, the approach based on Kirchhoff's would continue to provide a reliable result, even at quite small angles. This is an attractive advantage, balancing the increased computational effort. All results displayed in Figs. 14 and 15 lead to twofold outcomes, already seen in Fig. 10. Firstly, the number of azimuthal lobes, in the mid-span plane, increases with frequency, from only one when the airfoil chord is acoustically compact to up to three lobes in the investigated range at the highest frequency  $kc = 4\pi$ . Secondly, in non-compact cases, the number of azimuthal lobes decreases when going from the mid-span plane to high elevation angles.

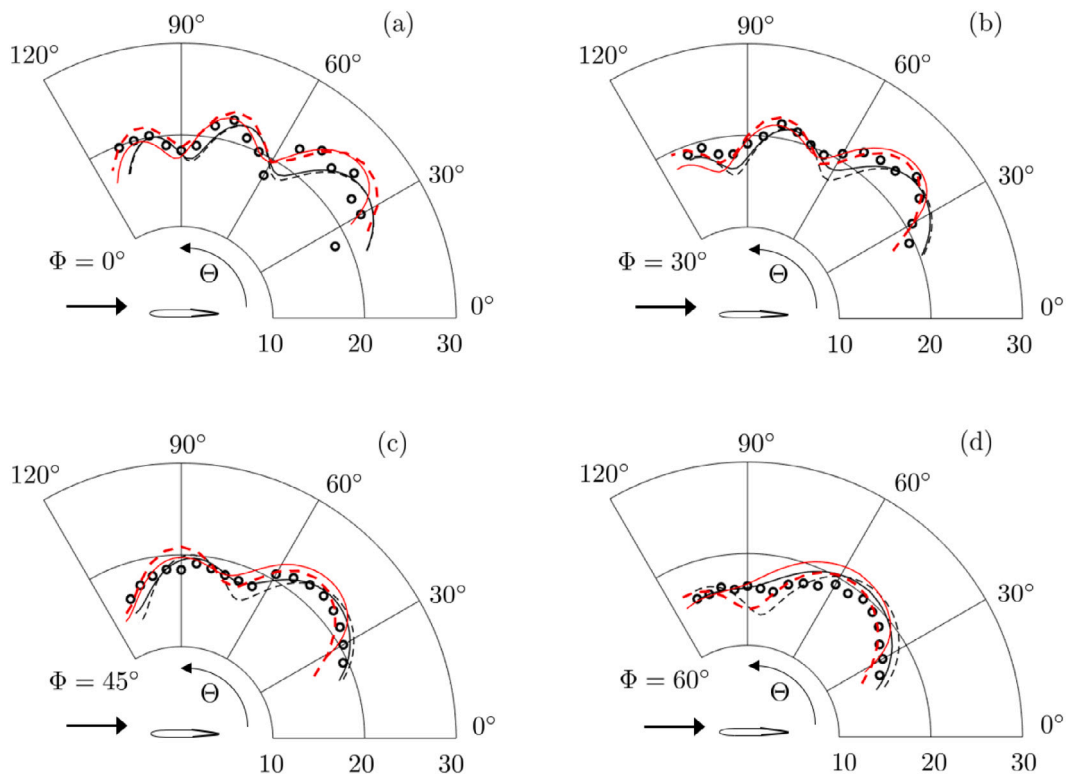


Fig. 14. Directivity patterns in azimuth  $\Theta$ , for various elevation angles  $\Phi = 0^\circ$  (a),  $30^\circ$  (b),  $45^\circ$  (c) and  $60^\circ$  (d).  $U_0 = 32$  m/s,  $kc = 4\pi$ . Measurements as symbols. Infinite-stream predictions as black lines, according to Eq. (1) (plain) and Eq. (2) (dashed). Corrected predictions from Eq. (1) according to Amiet's formulae (plain red). Predictions with Kirchhoff's formula as thick-dashed red lines. (For interpretation of the references to color in this figure legend, the reader is referred to the web version of this article.)

#### 4.4. Far-field spectra

Measured far-field sound spectra are compared with Amiet's predictions in Fig. 16, after shear-layer refraction correction. The latter is based on Amiet's abacuses, because repeated applications of Kirchhoff's formula for many frequencies would have been prohibitive. The comparison is made for the four  $\Theta$  angles  $30^\circ$ ,  $60^\circ$ ,  $90^\circ$  and  $110^\circ$ . For each, the results at three  $\Phi$  angles,  $0^\circ$ ,  $45^\circ$  and  $60^\circ$  are superimposed on the same plot. Pairs of predicted and measured spectra are shifted by multiples of 5 dB as indicated, for clarity. A very good agreement is found, with discrepancies below 1 dB over a wide range of frequencies and for most observation angles. Similar agreement has been observed for angles not reported in the figure.

The model predictions deviate from the measured data only below a low-frequency threshold of 300–500 Hz. The associated value of  $\mu = kc/(2\beta^2)$  is about 0.3, close to the validity limit of Amiet's high-frequency theory [15]. Furthermore, some contamination by the oscillations of the free shear layers of the nozzle jet are suspected at the lower frequencies, possibly making the measured data questionable. Amiet's model is finally fully validated in a three-dimensional context.

## 5. Conclusions

The experimental assessment of the turbulence-impingement noise (TIN) of a flat-plate airfoil at zero degree angle-of-attack and at a Reynolds number based on the chord of about  $2 \times 10^5$  has been achieved in the ECL small open-jet wind tunnel. TIN reduction by wavy leading-edge serrations has also been addressed. New data have been collected off the mid-span plane, providing the first three-dimensional experimental database on TIN and its mitigation by wavy serrations. This has been achieved by replacing the usual end-plate set-up with narrow support plates, making the airfoil acoustically visible from all observation angles and avoiding masking effects. The self-similarity of the flow and of its acoustic signature in the whole space has been verified, for both the straight-edge and serrated thin airfoils, by scaling the PSD of the far-field acoustic pressure with the velocity. Yet, in the serrated case, the TEN has been found to become significant beyond 4 kHz and to be substantially modified by the leading-edge serrations. When its contribution is removed, an almost monotonically increasing reduction  $\Delta_{dB}$  is found with increasing frequency, in a wide frequency range, for all radiation directions. Apart from irregularities explained by the chordwise non-compactness, a nearly linear increase of  $\Delta_{dB}$  with the logarithm of frequency is found. This trend remains close to the previously found noise gain of  $\Delta_{dB} = 10 \log_{10}(St_{h_s}) + 10$ , if  $St_{h_s}$  denotes the Strouhal number based on the serration depth, but the slope slightly decreases with increasing elevation angle,

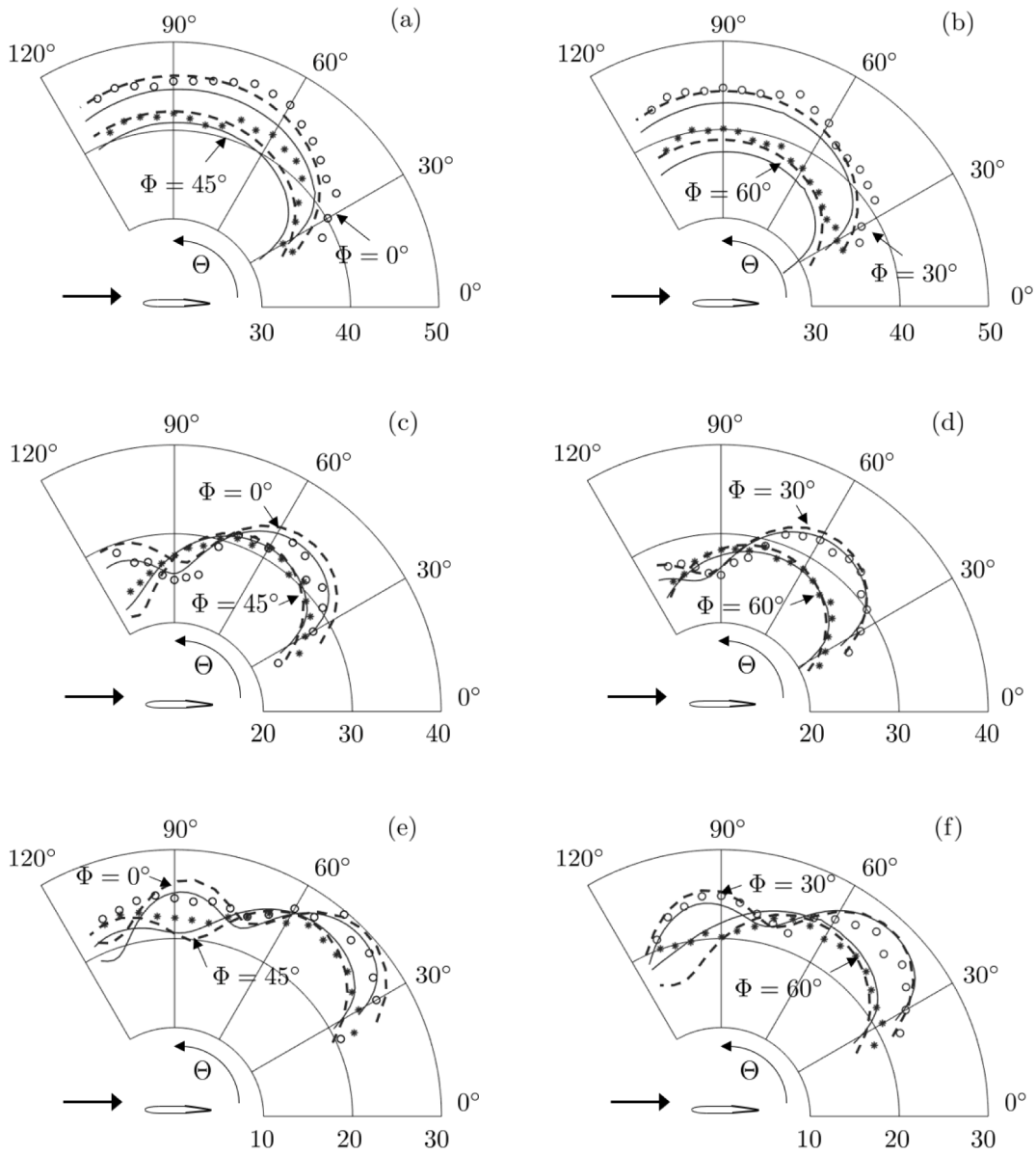


Fig. 15. Directivity patterns in azimuth  $\theta$ , for various elevation angles  $\Phi = 0^\circ, 45^\circ$  (a, c, e),  $\Phi = 30^\circ, 60^\circ$  (b, d, f).  $U_0 = 32 \text{ m/s}$ ,  $kc = \pi/2$  (a, b),  $kc = 2\pi$  (c, d),  $kc = 3\pi$  (e, f). Measurements as symbols. Infinite-stream predictions with Amiet's correction (thin plain lines) versus Kirchhoff's formula (thick-dashed black lines).

which provides an extension of the previously proposed fit off the midspan plane. This implies that TIN reduction is larger at high frequencies, and smaller at low frequencies, as the emission angle gets closer to the flow direction.

The far-field measurements with the straight-edge airfoil are also used to validate Amiet's analytical prediction model of TIN in a three-dimensional context for the first time. For this, a novel correction method based on Kirchhoff's integral theorem has been implemented to account for sound refraction through the shear layers of the nozzle jet, in the analytical predictions. The correction involves the lateral and upper shear layers directly seen from the arc microphones, both assimilated to zero-thickness plane interfaces. It is a frequency-dependent alternative to Amiet's ray-tracing approach, extending the range of the predictions into the zone of silence. At angles for which both are valid, the two methods provide similar results. For the present low-speed application, at a typical Mach number of 0.1, the amplitude correction is found moderate but the angle correction reaches  $5^\circ$  at all observer angles. Therefore, predictions aimed at comparing with measurements performed in open-jet anechoic facilities, should be systematically corrected for refraction effects, in order to ensure accuracy. In the present case, the corrected predictions are found in a remarkably good agreement with the measurements, both in terms of sound spectra and in terms of directivity. The advantage

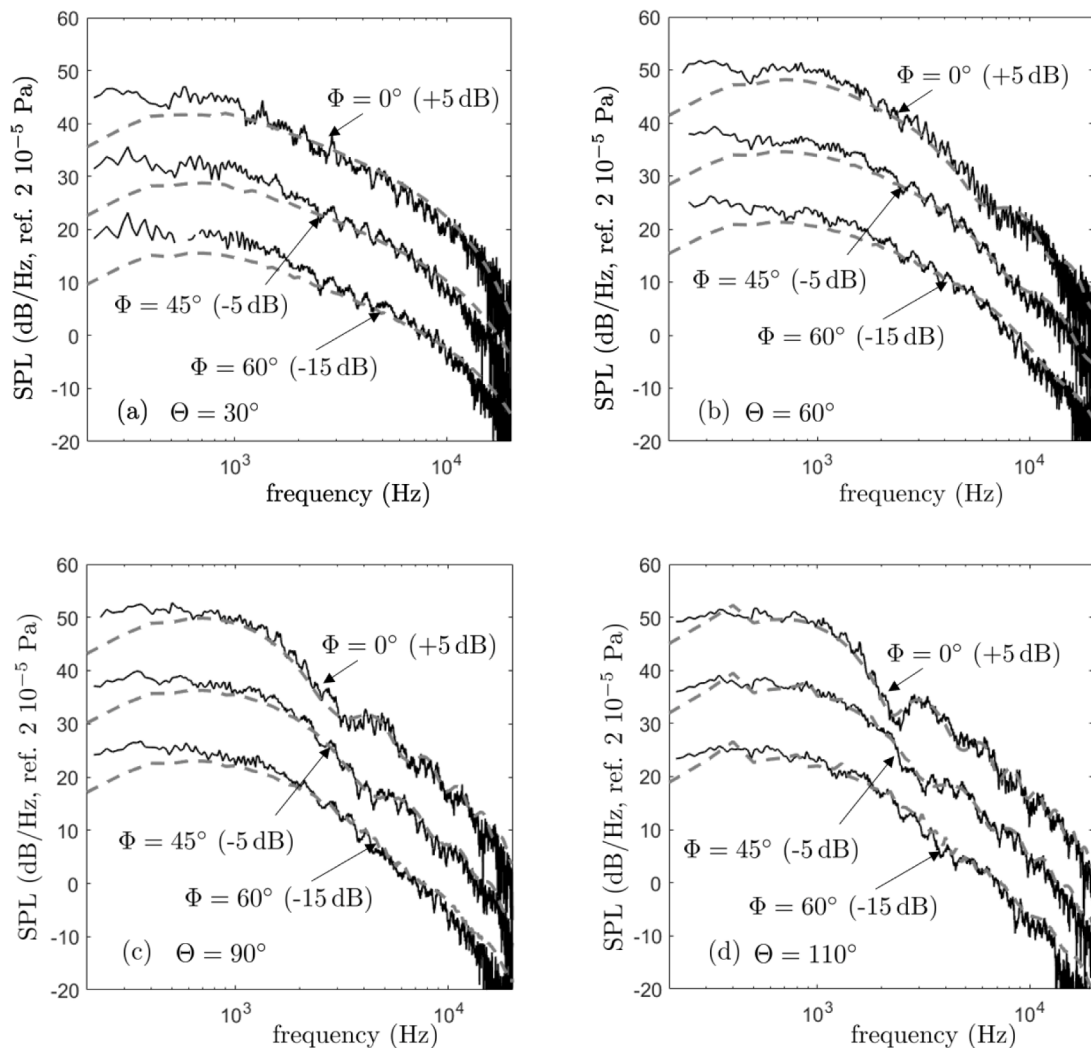


Fig. 16. Far-field sound spectra of turbulence-impingement noise.  $\theta = 30^\circ$  (a),  $60^\circ$  (b),  $90^\circ$  (c) and  $110^\circ$  (d). Elevation angles  $\Phi$  indicated on each plot.  $U_0 = 32$  m/s. Measurements (plain) versus Amiet's predictions (dashed gray).

of Kirchhoff's integral method is that it can be applied to shear layers of arbitrary shapes, and for arbitrarily extending source distributions. However, it is only applicable when a source model, valid in the flow region, is available.

#### CRediT authorship contribution statement

**Georgios Bampanis:** Conceptualization, Methodology, Data analysis, Analytics, Experiments, Validation, Formal analysis, Investigation, Data curation, Writing – original draft, Writing – review & editing, Visualization. **Michel Roger:** Conceptualization, Validation, Resources, Supervision, Analytics, Formal analysis, Writing – original draft, Visualization, Project administration, Writing – review & editing, funding acquisition. **Stéphane Moreau:** Conceptualization, Analytics, Formal analysis, Writing – original draft – review & editing, Supervision.

#### Declaration of competing interest

The authors declare that they have no known competing financial interests or personal relationships that could have appeared to influence the work reported in this paper.

## Acknowledgments

This study has received funding from the European Union's Horizon 2020 research and innovation programme under the Marie Skłodowska Curie, grant agreement No. 722401 (SmartAnswer). It was performed within the framework of the Labex CeLyA of the Université de Lyon, within the programme 'Investissements d'Avenir' (ANR-10-LABX-0060/ANR-11-IDEX-0007) operated by the French National Research Agency (ANR).

## References

- [1] D.S. Miklosovic, M.M. Murray, L.E. Howle, F.E. Fish, Leading-edge tubercles delay stall on humpback whale (*Megaptera novaeangliae*) flippers, *Phys. Fluids* 16 (2004) 39–42.
- [2] Y.Y. Wang, W.R. Hu, S.D. Zhang, Performance of the bio-inspired leading edge protuberances on a static wing and a pitching wing, *J. Hydrodyn.* 26 (2014) 912–920.
- [3] A. Corsini, G. Delibra, A.G. Sheard, The application of sinusoidal blade-leading edges in a fan-design methodology to improve stall resistance, *Proc. Inst. Mech. Eng. A* 228 (2014) 255–271.
- [4] F. Krömer, A. Renz, S. Becker, Experimental investigation of the sound reduction by leading-edge serrations in axial fans, *AIAA J.* 56 (2018) 2086–2090.
- [5] A.S. Lau, S. Haeri, J.W. Kim, The effect of wavy leading edges on aerofoil–gust interaction noise, *J. Sound Vib.* 332 (2013) 6234–6253.
- [6] S. Narayanan, P. Chaitanya, S. Haeri, P. Joseph, J.W. Kim, C. Polacsek, Airfoil noise reductions through leading edge serrations, *Phys. Fluids* 27 (2015) 025109.
- [7] P. Chaitanya, J.R. Gill, S. Narayanan, P. Joseph, C. Vanderwel, X. Zhang, B. Ganapathisubramani, Aerofoil geometry effects on turbulence interaction noise, in: 21st AIAA/CEAS Aeroacoustics Conference, AIAA Paper 2005-2830, 2015.
- [8] P. Chaitanya, P. Joseph, S. Narayanan, C. Vanderwel, J. Turner, J.W. Kim, B. Ganapathisubramani, Performance and mechanism of sinusoidal leading edge serrations for the reduction of turbulence-aerofoil interaction noise, *J. Fluid Mech.* 818 (2017) 435–464, <http://dx.doi.org/10.1017/jfm.2017.141>.
- [9] M. Roger, S. Moreau, Airfoil turbulence-impingement noise reduction by porosity or wavy leading-edge cut: Experimental investigations, in: INTER-NOISE and NOISE-CON Congress and Conference Proceedings, vol. 253, Institute of Noise Control Engineering, 2016, pp. 6366–6375.
- [10] G. Bampanis, M. Roger, Three-dimensional effects in the reduction of turbulence-impingement noise of aerofoils by wavy leading edges, in: Euronoise, 2018, pp. 97–104.
- [11] G. Bampanis, M. Roger, D. Ragni, F. Avallone, C. Teruna, Airfoil-Turbulence Interaction Noise Source Identification and its Reduction by Means of Leading Edge Serrations, in: 25th AIAA/CEAS Aeroacoustics Conference, AIAA Paper 2019-2741, Delft, Netherlands, 2019.
- [12] J.W. Kim, S. Haeri, P.F. Joseph, On the reduction of aerofoil-turbulence interaction noise associated with wavy leading edges, *J. Fluid Mech.* 792 (2016) 526–552.
- [13] P. Chaitanya, P. Joseph, S. Narayanan, J.W. Kim, Aerofoil broadband noise reductions through double-wavelength leading-edge serrations: A new control concept, *J. Fluid Mech.* 855 (2018) 131–151.
- [14] Y. Wang, K. Zhao, X.-Y. Lu, Y.-B. Song, G.J. Bennett, Bio-inspired aerodynamic noise control: A bibliographic review, *Appl. Sci.* 9 (2019) 2224.
- [15] R.K. Amiet, Acoustic radiation from an airfoil in a turbulent stream, *J. Sound Vib.* 41 (1975) 407–420.
- [16] R.K. Amiet, High frequency thin-airfoil theory for subsonic flow, *AIAA J.* 14 (1976) 1076–1082.
- [17] L. Landahl, *Unsteady Transonic Flow*, Pergamon Press, New York, 1961.
- [18] R.W. Paterson, R.K. Amiet, *Acoustic Radiation and Surface Pressure Characteristics of an Airfoil Due to Incident Turbulence*, Contractor Report CR-2733, NASA, 1976.
- [19] S. Moreau, M. Roger, V. Jurdic, Effect of angle of attack and airfoil shape on turbulence-interaction noise, in: 11th AIAA/CEAS Aeroacoustics Conference Meeting and Exhibit, Monterey, CA, AIAA 2005-2973 paper, Monterey, CA, 2005.
- [20] W.J. Devenport, J.K. Staubs, S.A.L. Glegg, Sound radiation from real airfoils in turbulence, *J. Sound Vib.* 329 (2010) 3470–3483.
- [21] J. Christophe, K. Kucukcoskun, C. Schram, A. Idier, P. Laffay, S. Moreau, Experimental validation of a semi-analytical trailing-edge noise model including broadband scattering, in: 21th AIAA/CEAS Aeroacoustics Conference, Dallas, TX, AIAA 2015-2531 paper, Dallas, TX, 2015.
- [22] M. Roger, On broadband jet-ring interaction noise and aerofoil turbulence-interaction noise predictions, *J. Fluid Mech.* 653 (2010) 337–364.
- [23] M. Tuinstra, S. Oerlemans, J.H.M. Gooden, Trailing Edge Noise: a Benchmark for PIV Based Noise Prediction, NLR-TP-2012-332 Report, National Aerospace Laboratory NLR, 2013.
- [24] S. Moreau, M. Roger, Back-scattering correction and further extensions of Amiet's trailing-edge noise model. Part II: Application, *J. Sound Vib.* 323 (2009) 397–425, <http://dx.doi.org/10.1016/j.jsv.2008.11.051>.
- [25] C. Schram, S. Moreau, M. Roger, Numerical modelling of realistic installation effects for airfoil broadband noise prediction and validation, in: Fan Noise 2007 International Symposium, Paper 36, Lyon, France, 2007.
- [26] S. Moreau, C. Schram, M. Roger, Diffraction effects on the trailing edge noise measured in an open-jet anechoic wind tunnel, in: 13th AIAA/CEAS Aeroacoustics Conference Meeting and Exhibit, Monterey, CA, AIAA 2007-3706 paper, Rome, Italy, 2007.
- [27] S. Moreau, M. Roger, Competing broadband noise mechanisms in low-speed axial fans, *AIAA J.* 45 (2007) 48–57.
- [28] S. Oerlemans, P. Migliore, Aeroacoustic wind-tunnel test of wind-turbine airfoils, in: 10th AIAA/CEAS Aeroacoustics Conference Meeting and Exhibit, Manchester, UK, vol. 8, 2004, pp. 555–584.
- [29] M. Roger, S. Moreau, Extensions and limitations of analytical airfoil broadband noise models, *Int. J. Aeroacoustics* 9 (2010) 273–305.
- [30] R.K. Amiet, Refraction of sound by a shear layer, *J. Sound Vib.* 58 (1978) 467–482.
- [31] R.H. Schlinker, R.K. Amiet, Shear-layer refraction and scattering of sound, in: 6th AIAA Aeroacoustics Conference, Hartford, CO, AIAA 80-0973 paper, 1980.
- [32] S.A.L. Glegg, W.J. Devenport, *Aeroacoustics of Low Mach Number Flow: Fundamentals, Analysis and Measurement*, Academic Press Elsevier, 2017.